



ALMA MATER STUDIORUM  
UNIVERSITÀ DI BOLOGNA

ARCHIVIO ISTITUZIONALE  
DELLA RICERCA

Alma Mater Studiorum Università di Bologna  
Archivio istituzionale della ricerca

Ganymede's Ionosphere observed by a Dual-Frequency Radio Occultation with Juno

This is the final peer-reviewed author's accepted manuscript (postprint) of the following publication:

*Published Version:*

Buccino, D.R., Parisi, M., Gramigna, E., Gomez Casajus, L., Tortora, P., Zannoni, M., et al. (2022).  
Ganymede's Ionosphere observed by a Dual-Frequency Radio Occultation with Juno. *GEOPHYSICAL  
RESEARCH LETTERS*, 49(23), 1-13 [10.1029/2022GL098420].

*Availability:*

This version is available at: <https://hdl.handle.net/11585/895452> since: 2024-05-15

*Published:*

DOI: <http://doi.org/10.1029/2022GL098420>

*Terms of use:*

Some rights reserved. The terms and conditions for the reuse of this version of the manuscript are specified in the publishing policy. For all terms of use and more information see the publisher's website.

This item was downloaded from IRIS Università di Bologna (<https://cris.unibo.it/>).  
When citing, please refer to the published version.

(Article begins on next page)

1  
2  
3  
4  
5  
6  
7  
8  
9  
10  
11  
12  
13  
14  
15  
16  
17  
18  
19  
20  
21  
22  
23

## **Ganymede's Ionosphere observed by a Dual-Frequency Radio Occultation with Juno**

**D. R. Buccino<sup>1</sup>, M. Parisi<sup>1</sup>, E. Gramigna<sup>2</sup>, L. Gomez-Casajus<sup>3</sup>, P. Tortora<sup>2,3</sup>, M. Zannoni<sup>2,3</sup>,  
A. Caruso<sup>2</sup>, R.S. Park<sup>1</sup>, P. Withers<sup>4</sup>, P. Steffes<sup>5</sup>, A. Hodges<sup>5</sup>, S. Levin<sup>1</sup>, S. Bolton<sup>6</sup>**

<sup>1</sup> Jet Propulsion Laboratory, California Institute of Technology

<sup>2</sup> Department of Industrial Engineering, Alma Mater Studiorum - Università di Bologna, Italy

<sup>3</sup> Centro Interdipartimentale di Ricerca Industriale Aerospaziale, Alma Mater Studiorum -  
Università di Bologna, Italy

<sup>4</sup> Boston University, Boston, MA

<sup>5</sup> School of Electrical and Computer Engineering, Georgia Institute of Technology

<sup>6</sup> Southwest Research Institute, San Antonio, Texas

Corresponding author: Dustin R. Buccino ([Dustin.R.Buccino@jpl.nasa.gov](mailto:Dustin.R.Buccino@jpl.nasa.gov))

### **Key Points:**

- A dual-frequency radio occultation experiment of Ganymede's ionosphere was conducted with the Juno spacecraft on June 7, 2021
- Ingress observed an ionosphere with peak density  $2000 \pm 500$  ( $1-\sigma$ )  $\text{cm}^{-3}$  but no statistically significant signature was detected on egress
- Ingress detection occurred in the open field line region, where higher electron impact ionization rates may increase the electron density

## 24 **Abstract**

25 In June 2021, the Juno spacecraft executed a close flyby of Ganymede. During the encounter, Juno  
26 passed behind Ganymede for 15 minutes as observed from Earth, providing the geometry to  
27 conduct a radio occultation experiment to probe Ganymede's tenuous ionosphere. X-band and Ka-  
28 band radio links were transmitted from Juno to antennas at the Deep Space Network. Electrons  
29 encountered along the radio propagation path advance the signal's phase and a linear combination  
30 the two frequencies allows for a direct measurement of the electron content along the propagation  
31 path. On occultation ingress, an ionosphere peak of  $2000 \pm 500$  ( $1-\sigma$ )  $\text{cm}^{-3}$  near the surface was  
32 observed. On occultation egress, no statistically significant ionosphere was detected. Ingress  
33 observation viewed where Ganymede's intrinsic magnetic field lines are open whereas egress  
34 observation viewed where the field lines are closed, implying electron impact ionization plays a  
35 key role in the generation of the ionosphere.

36

## 37 **Plain Language Summary**

38 Juno conducted a flyby of Ganymede, the largest Galilean moon of Jupiter, on June 7, 2021. During  
39 the flyby, the Juno spacecraft set behind Ganymede as observed by the Earth. Juno's radio signals  
40 were captured by the Deep Space Network during this time to make radio occultation  
41 measurements of Ganymede's ionosphere. Elevated electron density was measured on occultation  
42 ingress but no statistically significant ionosphere was detected on egress. These results are  
43 consistent with Galileo's radio occultation observations and provide insight into the generation  
44 mechanisms of Ganymede's ionosphere.

## 45 **1 Introduction**

46 The Galilean moons of Jupiter are known to have atmospheres and ionospheres, detected  
47 with both ground-based observations and spacecraft data. An oxygen-hydrogen atmosphere was  
48 discovered on Ganymede with observations by the Hubble Space Telescope (Hall et al., 1998).  
49 Ganymede is a unique object in the solar system in that it has its own intrinsic magnetic field which  
50 interacts with the Jovian magnetosphere (Kivelson et al, 1997). Within the open field line regions  
51 at higher latitudes, sputtering generates an atmosphere of molecular oxygen subject to ionization  
52 and dissociated excitation from the Jovian magnetosphere (Eviatar et al., 2001). Within closed  
53 field line regions, it is expected the atmosphere is produced by sublimation (Alexander et al.,  
54 1999). It is thought the ionosphere is generated from the neutral atmosphere via photoionization  
55 and electron impact from the Jovian magnetosphere (Carnielli et al., 2019). Prior to Juno's  
56 encounter with Ganymede, the only direct measurements of Ganymede's ionosphere were those  
57 acquired in-situ measurements from the Galileo particle detectors and by the Galileo radio  
58 occultation experiment. Due to the flyby distance of the in-situ spacecraft measurements, radio  
59 occultation data provide valuable information about the electron densities near the surface of  
60 Ganymede.

61 The Galileo spacecraft executed a total of eight S-band radio occultations of Ganymede  
62 throughout its mission, resulting in five non-detections, two weak detections, and one strong  
63 detection of an ionosphere (McGrath et al., 2004). To the best of our knowledge, the Galileo radio  
64 science data at Ganymede were never archived. In particular with respect to Ganymede, only  
65 occultation profiles from the G8 encounter were ever published in scientific literature. The strong  
66 ionosphere detection occurred during the Ganymede G8 egress occultation resulting in a peak

67 electron density of  $\sim 5000 \text{ cm}^{-3}$  near the surface (Kliore, 1998). Initially, the lack of detection was  
68 surprising, but it was hypothesized that positive detections occurred where the trailing hemisphere  
69 (where the magnetospheric plasma impacts the moon) of the satellite was in sunlight; therefore,  
70 the atmosphere created by sputtering effects from the Jovian magnetosphere can be can be ionized  
71 by solar radiation to produce an observable ionosphere (Kliore et al., 2001).

72 On June 7, 2021, the Juno spacecraft performed a close flyby of Ganymede (Hansen et al.,  
73 2022). During this flyby, the spacecraft was occulted by Ganymede as viewed from Earth.  
74 Coherent radio links were established during the flyby to enable a radio occultation experiment  
75 and gravity experiment to investigate the interior structure (Gomez-Casajus et al., 2022). This  
76 article presents the analysis and results of Juno's radio occultation experiment at Ganymede. It is  
77 concluded with an interpretation of the resultant ionospheric electron density profiles in the context  
78 of current knowledge of Ganymede's tenuous atmosphere and variable ionosphere.

## 79 **2 Occultation Experiment with Juno**

80 The Juno Gravity Science Instrument (Asmar et al., 2017) is a radio science instrument  
81 which utilizes dual-frequency X-band (8.4 GHz) and Ka-band (32 GHz) radio links between the  
82 Juno spacecraft and the Earth-based observing stations of NASA's Deep Space Network (DSN).  
83 On June 7, 2021 Juno's extended mission trajectory took the spacecraft on a close encounter with  
84 Ganymede at an altitude of 1045 km. An Earth occultation occurred during this flyby as shown in  
85 Figure 1. Geometric information is summarized in Table 1. Measurement of Ganymede's  
86 ionosphere is made via a radio occultation geometry, where the Juno spacecraft set behind  
87 Ganymede as observed from Earth. In this way, the radio ray path propagates directly through the  
88 ionosphere of Ganymede twice, once on ingress and once on egress. During the radio occultation,  
89 Juno transmitted dual-frequency X-band and Ka-band to the 70-meter DSS-43 and 34-meter DSS-  
90 35 antennas at the Canberra DSN complex. The occultation experiment was executed in a coherent  
91 mode with the downlink signal coherent with the uplink. Both downlink signals were referenced  
92 to a single X-band uplink signal sent from the DSS-35 antenna.

93 Several hours prior to occultation, the DSS-35 antenna transmitted an X-band uplink signal  
94 to the spacecraft with a typical uplink acquisition sweep. The acquisition sweep transmits a range  
95 of frequencies ( $\pm 10 \text{ kHz}$  at  $200 \text{ Hz/sec}$ ) around the spacecraft transponder's best lock frequency  
96 which takes 170 seconds to execute. The transponder locked to this signal and phase-coherently  
97 transmitted X-band and Ka-band back to Earth at ratios of 880/749 and 3360/749, respectively.  
98 Upon occultation ingress, the transponder unlocked from the uplink signal due to the loss of signal.  
99 In order to re-acquire the signal as quickly as possible on egress, a "snap-lock" technique was  
100 utilized. In a snap-lock, an uplink acquisition sweep is not executed and instead relies on precisely  
101 targeting the spacecraft transponder's best lock frequency to within the pull-in range of 1.3 kHz.  
102 For this technique, two effects are carefully considered: a prediction of the oscillator frequency  
103 based upon the temperature of the oscillator; and a prediction of the estimated Doppler shift in the  
104 uplink signal. The snap-lock on egress was successful and the transponder re-locked to the uplink  
105 signal less than 1 second after geometric occultation egress (corresponding with  $\sim 5.9 \text{ km}$  in  
106 altitude). Due to the fast flyby velocity ( $\sim 18.6 \text{ km/sec}$ ), without a snap-lock, egress occultation  
107 data would have been lost.

### 108 **3 Methodology**

109 Radio occultation experiments are well-known planetary science methods widely used to  
110 perform remote sensing of planetary atmospheres of Solar System bodies, in particular to retrieve  
111 vertical profiles of ionosphere electron density and neutral atmosphere physical quantities. The  
112 basics of radio occultation experiments for planetary science applications have been presented by  
113 (Fjeldbo and Eshleman, 1965; Kliore et al., 1965; Fjeldbo and Eshleman, 1968; Phinney and  
114 Anderson, 1968; Fjeldbo et al., 1971). In this technique, the spacecraft transmits a radio signal  
115 from the onboard radio to Earth, where it is received by a large ground antenna. As the spacecraft  
116 sets behind an object, as viewed from Earth, the radio link will propagate through the object's  
117 atmosphere and ionosphere, and it experiences refraction. While investigating ionospheres,  
118 refraction due to electrons encountered along the radio ray path causes the signal to bend towards  
119 regions of higher index of refraction. This bending produces a phase change in the radio signal  
120 proportional to the electron content encountered along the ray path, and it is measured by the  
121 ground receiver as a frequency shift. In this context, a dual-frequency analysis is particularly  
122 powerful, since it isolates the effect of free-electrons and allows to derive the total electron content  
123 and, under certain hypotheses, the local electron density. This analysis adapts methodology as  
124 described by Phipps and Withers (2017) and Dalba and Withers (2019) which is briefly described  
125 in the following sections.

#### 126 **3.1 Signal Processing**

127 Radio Science utilizes radiometric tracking data collected by the DSN. The preferred  
128 method for radio occultation experiments utilizes the Open-Loop Receivers (OLR). The OLR  
129 digitally down-converts and records the full spectrum at a user-defined sample rate. The OLR  
130 relies on predicted downlink frequencies based on the Doppler shift caused by the motion of the  
131 spacecraft trajectory to remain tuned to the incoming signal, without having a feedback loop to be  
132 used to track and lock the received signal. This is particularly advantageous in radio occultation  
133 experiments, where it is challenging to establish and/or maintain the signal lock near the surface  
134 where the signal will be lost and re-acquired. Occultation data were processed from open-loop  
135 recordings at 1 kilosamples per second (in-phase and quadrature). The frequency time series are  
136 retrieved by processing the OLR data through a spectral fast-Fourier transform algorithm (Paik  
137 and Asmar, 2011), in order to obtain a sufficiently high number of frequency measurements. Due  
138 to the fast flyby of Ganymede by Juno, the integration time-step of 1 second was selected. This  
139 resulted in a satisfactory trade-off between the number of measurements in order to have enough  
140 vertical resolution to probe Ganymede's tenuous ionosphere, and the thermal noise.

#### 141 **3.2 Differential Frequency Technique**

142 The differential frequency, or dual-frequency, technique uses two frequencies  
143 simultaneously to determine the structure of a planetary body's ionosphere. This method allows  
144 for the removal of the classical Doppler shift, as well as the non-dispersive effects, such as neutral  
145 atmosphere contributions, and the time variation of the uplink frequency as seen by the spacecraft  
146 (clock source). In this way it is possible to isolate the effect of free electrons, which is frequency  
147 dependent, on rays traversing the ionosphere.

148 As shown in Equation 1 (Dalba and Withers, 2020), the received frequency,  $f_R$ , differs from  
149 the transmitted frequency,  $f_T$ . This is due to the classical Doppler shift (which can be computed  
150 using Equation 1 of Schinder et al. 2015), a shift due to plasma along the ray path, and a shift due  
151 to neutral gas along the ray path, respectively. The frequency shift due to the charged particles is

152 inversely proportional to the transmit frequency  $f_T$ . In this way, it is possible to take advantage of  
 153 multiple frequencies to directly measure the electron content along the radio ray path.

$$f_R = f_T - \frac{f_T}{c} \frac{d}{dt} \int dl + \frac{e^2}{8\pi^2 m_e \epsilon_0 c f_T} \frac{d}{dt} \int N_e dl - \frac{f_T \kappa}{c} \frac{d}{dt} \int n dl \quad (1)$$

154 where  $l$  is the path length,  $c$  is the speed of light,  $t$  is time,  $e$  is the elementary charge,  $m_e$  is  
 155 the electron mass,  $\epsilon_0$  is the permittivity of free space,  $N_e$  and  $n$  are the electron density and neutral  
 156 density at a given point, respectively, and  $\kappa$  is the refractive volume of neutral gas at a given point.

157 During the occultation, the spacecraft transmitted frequencies at X-band ( $f_{T,X}$ ) and at Ka-  
 158 band ( $f_{T,Ka}$ ). The frequencies precisely related by the ratio of the turnaround ratios, i.e.  $f_{T,Ka}/f_{T,X} =$   
 159  $3360/880$ . Differential frequency residuals are then obtained as a function of time in Equation 2.

$$\Delta f(t) = f_{R,X}(t) - \frac{880}{3360} f_{R,Ka}(t) = \frac{e^2}{8\pi^2 m_e \epsilon_0 c f_{T,X}} \left( 1 - \left( \frac{880}{3360} \right)^2 \right) \frac{d}{dt} \int N_e dl \quad (2)$$

160 As a result, the plasma column density along the ray path  $\int N_e dl$ , or Total Electron Content  
 161 (TEC), as a function of time, can be directly obtained from time series of received frequencies at  
 162 X- and Ka-band. Because the dual-frequency link is only present on the downlink, the retrieved  
 163 TEC is referred to the downlink radio ray path only.

164 Before obtaining the TEC and local electron density, it is crucial to calibrate the differential  
 165 frequency residuals of Equation 2 for the solar plasma and Earth's ionosphere, in order to obtain  
 166 reliable results. If not calibrated, these effects could jeopardize the accuracy of the retrieved  
 167 electron densities. The noises can be evaluated in the baseline of the residual frequencies, the  
 168 region where the signal is traveling outside the ionosphere of Ganymede. The baseline should be  
 169 flat with low-noise and zero-mean residual frequencies. In the case of Juno, the largest effect on  
 170 the dual-frequency residuals is that of the spin-phase wrapping (Marini, 1971). A bias offset is  
 171 evaluated in the baseline and subtracted to the entire observation time-span of the differential  
 172 frequency residuals.

173 After calibration, Equation 2 is integrated with respect to time and obtain the TEC using  
 174 Equation 3. This is then translated into a function of the closest approach distance of the radio ray  
 175 path to the center of mass of Ganymede using the spacecraft and planetary ephemerides, where  $X$   
 176 is the closest approach distance.

$$TEC(X) = \int N_e dl = \int \frac{8\pi^2 m_e \epsilon_0 c f_{T,X}}{e^2 \left( 1 - \left( \frac{880}{3360} \right)^2 \right)} \Delta f(t) dt \quad (3)$$

177 Following (Dalba and Withers, 2020), and assuming that Ganymede's ionosphere is locally  
 178 spherically symmetric, the vertical profiles of Ganymede's electron density are obtained using an  
 179 Abel transform inversion formula, starting from the TEC (Fjeldbo et al., 1971; Hinson et al., 1999;  
 180 Withers, 2020) using Equation 4.

$$N_e(r) = \frac{1}{\pi} \int_{X=r}^{X=\infty} \ln \left( \frac{X}{r} + \sqrt{\left(\frac{X}{r}\right)^2 - 1} \right) d \left( \frac{dTEC(X)}{dX} \right) \quad (4)$$

181 where  $r$  is the radial distance. Consequently, the vertical profile of the ionospheric electron  
 182 density  $N_e(r)$ , is derived from the integrated plasma column density (TEC). In the Abel transform,  
 183 it is assumed that the ionosphere is spherically symmetric at the occultation point. The non-  
 184 spherical nature of Ganymede's ionosphere could possibly lead to biases in electron density results  
 185 at the icy moons of Jupiter in certain geometries (Kliore 1998). However, since the index of  
 186 refraction of the ionosphere is very small (it deviates from 1 by about  $10^{-9}$  in the part of the  
 187 ionosphere where the electron density is maximum), the rays do not bend significantly and they  
 188 can safely be assumed to follow straight lines. Thus, the Abel transform should still result in  
 189 accurate electron density profiles, for example, as assumed for Saturn and Titan (Schinder 2020).

## 190 4 Results

191 The analysis of the ingress leg of the experiment uses data beginning at 16:48:00.0 after  
 192 spacecraft telemetry was turned off, until 17:18:55.1. Although actual loss of signal at Ka-band  
 193 occurs 1 second later at 17:18:56.1, effects of diffraction are observed and the data cutoff was  
 194 chosen to occur prior to this (see Text S1 of Supporting Information). The egress leg consists of  
 195 data between the time of signal re-acquisition at 17:32:38.0 until the 17:52:00.0 when a second re-  
 196 acquisition sweep was executed. All times are stated in UTC as received on Earth (Earth Receive  
 197 Time). Because it took the spacecraft transponder  $\sim$ 1-2 seconds to re-acquire the uplink signal on  
 198 egress, and the non-coherent portion was not used, diffraction does not affect egress.

199 The ingress occultation occurred in the southern hemisphere of the moon at latitude  $59^\circ$ S,  
 200 while the egress occultation occurred 15 minutes later in the northern hemisphere at latitude  $20^\circ$ N.  
 201 In terms of magnetospheric geometry, both ingress and egress occurred near the terminator. The  
 202 egress occultation point was partially sun-lit as well as contained in Ganymede's magnetospheric  
 203 wake. As a result, ingress was characterized by a small Ram angle, and egress by a small Solar  
 204 Zenith angle, and either one (if not both) of these conditions are considered favorable for the  
 205 detection of an ionosphere.

206 Figure 2 shows the dual-frequency residuals (in Hz), which were obtained using Equation  
 207 2 for ingress (panel a) and egress (panel b). The data were calibrated as described in the previous  
 208 section, using a baseline defined by ray-path altitudes over Ganymede's surface between 5,000-  
 209 11,000 km for ingress, and 5,000-7,000 km for egress. These altitude intervals were selected so  
 210 that the baselines are completely outside of Ganymede's ionosphere. Nevertheless, the results are  
 211 stable regardless of the baseline chosen to perform the calibrations, down to an altitude of about  
 212 1,500 km.

213 After calibration, the profiles of dual-frequency residuals are directly converted using  
 214 Equation 3 into profiles of Total Electron Content (TEC), a measure of column density of electrons  
 215 ( $10^{16} \text{ m}^{-2}$ ). The TEC shows there is a clear accumulated ionosphere signal at low altitudes below  
 216 800 km during the ingress occultation but such signal is not detected on the egress occultation,  
 217 which remains relatively constant (see Figure S4 in Supporting Information).

218 The TEC represents the column density obtained integrating the electron density  $N_e$  along  
 219 the ray path, and is, therefore, an average measurement. To retrieve the local electron density (in

220  $\text{cm}^{-3}$ ) as a function of altitude, an Abel transform is performed on the TEC profile using Equation  
 221 4. The key assumption for using this algorithm is that of local spherical symmetry of the satellite  
 222 around the occultation point. The electron density is plotted once again against the altitude above  
 223 the surface of the satellite (Figure 3). For both ingress and egress the vertical resolution is  $\sim 5.9$  km  
 224 (at 1 second integration time) which is largely dependent on the flyby velocity. In order to mitigate  
 225 the effect of thermal noise, 1000 electron density profiles were generated by beginning the  
 226 frequency estimation with subsequent open-loop samples (1000 profiles are generated with a  
 227 sampling rate of 1 kHz). The profiles were then averaged (see Text S2 in Supporting Information).  
 228 These results show that there is an elevated electron density near the surface above the  $3\text{-}\sigma$   
 229 uncertainty level on ingress (Figure 3a). The peak density is approximately  $(2000 \pm 500) \text{ cm}^{-3}$  ( $1\text{-}\sigma$ )  
 230 at a 15 km data cutoff altitude. On ingress between 15 km and 1,500 km, the corresponding  
 231 scale height  $H$  assuming an exponential ionosphere ( $e^{-z/H}$ ) is  $1050 \pm 110$  km. Egress yielded an  
 232 observation of  $(400 \pm 500) \text{ cm}^{-3}$  ( $1\text{-}\sigma$ ). Although the electron density profile on egress was more  
 233 sensitive to the calibration techniques, the averaged profile is statistically compatible with zero at  
 234 the  $3\text{-}\sigma$  level with one exception around 1,800 km. Due to the high altitude and sensitivity to the  
 235 baseline calibration, is likely not associated with the ionosphere and therefore we conclude egress  
 236 does not show a detection of an ionosphere (Figure 3b).

237 Thermal, instrumental, and propagation noise sources are present in the data. The  
 238 dominating noise in the observation is thermal. Instrumental noise is negligible, since the oscillator  
 239 stability and atmospheric effects cancel in the dual-frequency combination, leaving only hardware-  
 240 related sources with estimated Allan deviation stability on the order of  $\sim 10^{-16}$  to  $\sim 10^{-15}$  at 1000-sec  
 241 (Asmar et al 2005). Propagation sources of error from plasma are also present and include  
 242 fluctuations in the Earth's ionosphere and solar plasma. The local time of the ray path through  
 243 Earth's ionosphere occurred during night, when ionosphere activity is lower than daytime. These  
 244 variations in Earth's ionosphere during the occultation timeframe were small as measured by  
 245 GNSS receivers located at the DSN antennas. When calibrated, it did not change the results. Solar  
 246 plasma noise is the other propagation noise source. The larger drift trend of solar plasma is  
 247 removed in the background polynomial fit. Solar plasma scintillation at the solar elongation angle  
 248 of  $105^\circ$  during Ganymede's occultation corresponds with an X-band scintillation noise of 0.75  
 249 mHz (after conversion from Asmar et al (2005) from Allan deviation of  $\sim 2 \times 10^{-14}$  at 1000-sec),  
 250 therefore we do not expect this effect to dominate the data noise when compared with the thermal  
 251 noise levels of nearly twice that. However, undesired solar plasma noise may still be present in the  
 252 observation. The error bars (represented by shaded regions) were estimated through means of a  
 253 Monte Carlo analysis by adding gaussian random noise time-series (whose  $\sigma$  is consistent with the  
 254 observed noise outside Ganymede's ionosphere) to the original differential frequency residuals, in  
 255 order to obtain the standard deviations of the profiles in terms of electron density. The  $1\text{-}\sigma$  ( $\sim 500$   
 256  $\text{cm}^{-3}$ ) and  $3\text{-}\sigma$  uncertainties ( $\sim 1500 \text{ cm}^{-3}$ ) derived from the Monte Carlo analysis is consistent with  
 257 an uncertainty estimated using the method described by Withers, 2020.

## 258 5 Discussion

259 Ganymede's atmosphere is generated by charged particle sputtering and sublimation from  
 260 the icy surface with detections by Hubble Space Telescope (Hall et al, 1998 & Roth et al, 2021).  
 261 In the context of the Juno occultation measurements, ingress and egress occultation points appear  
 262 to be in ice-rich regions (Ligier et al., 2019) where this can occur. Ganymede's ionosphere is  
 263 generated from the neutral atmosphere through photo-ionization and electron-impact ionization



264 from Jupiter's magnetosphere (Carnielli et al., 2019). Juno's radio occultation are observed at the  
265 closest point to the surface of Ganymede along the ray path between the spacecraft and Earth. In  
266 this geometry, ingress was in the shadow whereas egress was in a sun-lit region (Figure 1). When  
267 comparing occultation points with open-closed field line boundaries of Ganymede's  
268 magnetosphere (either from Duling et al (2022) or Jia and Kivelson, 2021), it is evident that ingress  
269 occurred in the open-field line region and egress likely occurred in the closed-field line regions.  
270 Since electron-impact ionization rates would be higher in open field-line regions, the Juno  
271 occultation sheds light on the generation mechanisms for Ganymede's ionosphere.

272 The stark contrast in the geometry of the Juno occultation – ingress in the shadow, but open  
273 field-line and egress sun-lit, but in closed field-line region – indicates that electron-impact  
274 ionization plays an important role in generating Ganymede's ionosphere in the open-field line  
275 region. This is corroborated by the strong detection of the ionosphere by Galileo radio occultation.  
276 The G8 egress occultation, occurring at a latitude of  $47^\circ$  N and west longitude of  $22^\circ$  (Kliore 1998),  
277 was also in the open field-line region defined by Jia and Kivelson, 2021.

278 Previous modeling efforts of Ganymede's ionosphere have been conducted by Eviatar et  
279 al 2001, Carnielli et al 2019, and Carnielli et al 2020. Eviatar et al 2001 modeled the surface density  
280 of electrons is about  $400 \text{ cm}^{-3}$  with a scale height of 600 km. Near the surface, the scale height may  
281 be considerably smaller yielding a higher surface density. Although the modeled surface density  
282 is well below an upper limit obtained by the Galileo radio occultation measurement, Eviatar et al  
283 2001 also show that the peak electron densities measured by Kliore (1998) do not contradict a  
284 model of the ionosphere in the polar cap region due to large uncertainties in atomic and  
285 environmental parameters. Juno's ingress occultation observation of  $2000 \text{ cm}^{-3}$  is lower than the  
286 upper limit set by Galileo G8 egress occultation and thus the Juno occultation results not exclude  
287 this upper limit from possibilities either. Extending on Carnielli et al 2019, Carnielli et al 2020  
288 proposed that increasing neutral atmosphere densities or increased electron-impact ionization rates  
289 can explain discrepancies between observations and models.

290 Juno successfully executed a radio occultation of Ganymede during a close encounter on  
291 June 7, 2021. Both ingress and egress electron profiles were obtained using a dual-frequency  
292 technique. On ingress, an ionosphere signature was detected with a peak electron density of  $2000$   
293  $\pm 500$  ( $1-\sigma$ )  $\text{cm}^{-3}$  at 15 km with a scale height of  $1050 \pm 110$  km. On egress, no statistically  
294 significant ionosphere was detected. Thus, at first glance the Juno occultation results appears  
295 consistent with results of the Galileo occultation campaign where only one strong detection of an  
296 ionosphere was observed with a peak of approximately  $5000 \text{ cm}^{-3}$  at 16 km (Kliore 1998) out of  
297 eight occultation profiles. With current knowledge of the interaction between Ganymede's  
298 atmosphere, ionosphere, and Jupiter's magnetosphere, we conclude that the reason for the ability  
299 to detect an ionosphere with the radio occultation technique is due to higher electron impact  
300 ionization rates in open-field line regions, where positive detections of the ionosphere occur.

### 301 **Acknowledgments**

302 The work of DB, MP, RP, and SL was carried out at the Jet Propulsion Laboratory, California  
303 Institute of Technology, under a contract with the National Aeronautics and Space Administration.  
304 Government sponsorship acknowledged.

305  
306 EG, LGC, PT, MZ and AC are grateful to the Italian Space Agency (ASI) for financial support  
307 through Agreement No. 2018-25-HH.0 in the context of ESA's JUICE mission, and Agreement

308 No. 2017-40-H.1-2020, and its extension 2017-40-H.02020-13-HH.0, for ESA's BepiColombo  
 309 and NASA's Juno radio science experiments. EG is grateful to "Fondazione Cassa dei Risparmi  
 310 di Forlì" for financial support of his PhD fellowship.

311  
 312 PS and AH were supported by NASA Contract NNM06AA75C from the Marshall Space Flight  
 313 Center under subcontract 699054X from Southwest Research Institute.

314  
 315 © 2021 California Institute of Technology. Government sponsorship acknowledged.

### 316 **Data Availability Statement**

317 The Juno radio science data used in this research are publicly available through NASA's Planetary  
 318 Data System at [https://atmos.nmsu.edu/PDS/data/jnogrv\\_1001/](https://atmos.nmsu.edu/PDS/data/jnogrv_1001/) (Buccino, 2016). The occultation  
 319 results presented here are provided in a corresponding dataset with this publication on Zenodo  
 320 (Buccino, 2022).

### 321 **References**

322 Asmar, S. W., Armstrong, J. W. & Tortora, P. (2005). Spacecraft Doppler tracking: Noise budget  
 323 and accuracy achievable in precision radio science observations. *Radio Science*, 40(2), RS2001.

324 Asmar, S. W., Bolton, S. J., Buccino, D. R., Cornish, T. P., Folkner, W. M., Formaro, R., ... &  
 325 Simone, L. (2017). The Juno gravity science instrument. *Space Science Reviews*, 213(1), 205-218.

326 Buccino, D. R. (2016). Juno Jupiter gravity science raw data set V1.0, JUNO-J-RSS-1 JUGR-  
 327 V1.0, NASA planetary data system (PDS). Retrieved from  
 328 [https://atmos.nmsu.edu/PDS/data/jnogrv\\_1001/](https://atmos.nmsu.edu/PDS/data/jnogrv_1001/)

329 Dustin Buccino. (2022). Corresponding Dataset for Ganymede's Ionosphere observed by a Dual-  
 330 Frequency Radio Occultation with Juno [Data set]. <https://doi.org/10.5281/zenodo.6206226>

331 Carnielli, G., Galand, M., Leblanc, F., Leclercq, L., Modolo, R., Beth, A., ... & Jia, X. (2019). First  
 332 3D test particle model of Ganymede's ionosphere. *Icarus*, 330, 42-59.

333 Carnielli, G., Galand, M., Leblanc, F., Modolo, R., Beth, A., & Jia, X. (2020). Constraining  
 334 Ganymede's neutral and plasma environments through simulations of its ionosphere and Galileo  
 335 observations. *Icarus*, 343, 113691.

336 Dalba, P. A., & Withers, P. (2019). Cassini radio occultation observations of Titan's ionosphere:  
 337 The complete set of electron density profiles. *Journal of Geophysical Research: Space*  
 338 *Physics*, 124(1), 643-660.

339 Duling, S., Saur, J., et al (2022). Ganymede MHD Model: Magnetospheric Context for Juno's  
 340 PJ34 flyby. *Geophysical Research Letters*, xxx(x), xxx-xxx. (this issue)

341 Eviatar, A., Vasyliūnas, V. M., & Gurnett, D. A. (2001). The ionosphere of Ganymede. *Planetary*  
 342 *and Space Science*, 49(3-4), 327-336.

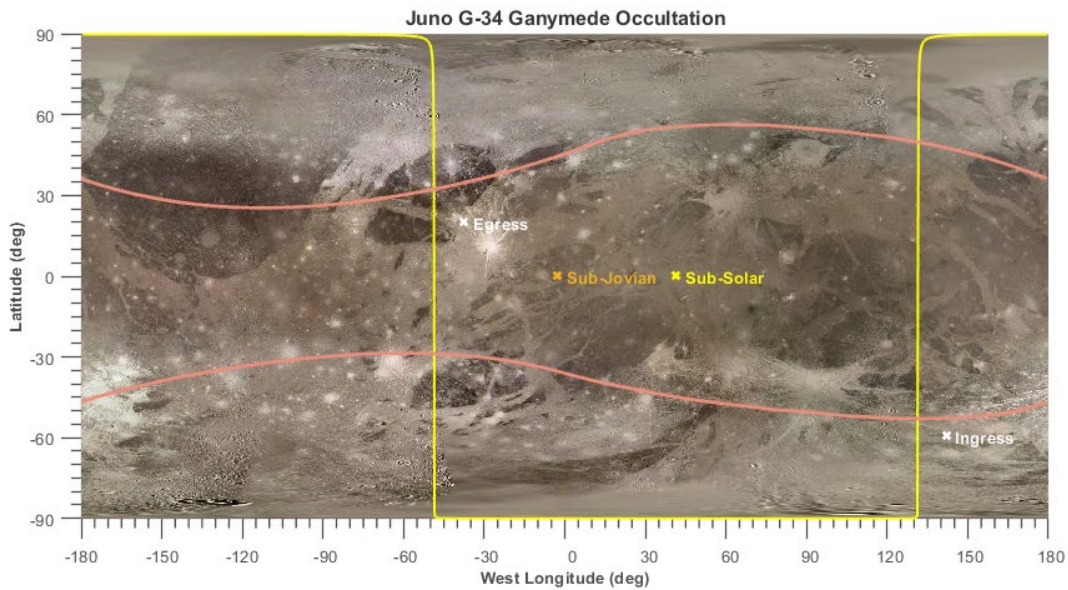
343 Fjeldbo, G. & Eshleman V. R., (1965). The bistatic radar-occultation method for the study of  
 344 planetary atmospheres. *Journal of Geophysical Research*, 70, 3217.

345 Fjeldbo, G., & Eshleman, V. R. (1968). The atmosphere of Mars analyzed by integral inversion of  
 346 the Mariner IV occultation data. *Planetary and Space Science*, 16(8), 1035-1059.

- 347 Fjeldbo, G., Kliore, A. J., & Eshleman, V. R. (1971). The neutral atmosphere of Venus as studied  
348 with the Mariner V radio occultation experiments. *The Astronomical Journal*, 76, 123.
- 349 Gomez-Casajus, et al (2022). The Gravity Field of Ganymede after the Juno's Extended Mission.  
350 *Geophysical Research Letters*, xxx(x), xxx-xxx. (this issue)
- 351 Hall, D. T., Feldman, P. D., McGrath, M. A., & Strobel, D. F. (1998). The far-ultraviolet oxygen  
352 airglow of Europa and Ganymede. *The Astrophysical Journal*, 499(1), 475.
- 353 Hansen, C.J., Bolton, S., Brennan, M., Lunine, J. Sulaiman, A., Levin, S., Connerney, J. and Clark  
354 G.P., Overview of Juno's Flyby of Ganymede. *Geophysical Research Letters*, xxx(x), xxx-xxx.  
355 (this issue)
- 356 Hinson, D. P., Simpson, R. A., Twicken, J. D., Tyler, G. L., & Flasar, F. M. (1999). Initial results  
357 from radio occultation measurements with Mars Global Surveyor. *Journal of Geophysical*  
358 *Research*, 104, 26,997–27,012
- 359 Jia, X., & Kivelson, M. G. (2021). The Magnetosphere of Ganymede. *Magnetospheres in the Solar*  
360 *System*, 557-573.
- 361 Kivelson, M. G., Khurana, K. K., Coroniti, F. V., Joy, S., Russell, C. T., Walker, R. J., ... &  
362 Polanskey, C. (1997). The magnetic field and magnetosphere of Ganymede. *Geophysical*  
363 *Research Letters*, 24(17), 2155-2158.
- 364 Kliore, A. J. (1998). Satellite atmospheres and magnetospheres. *Highlights of Astronomy*, 11(2),  
365 1065-1069.
- 366 Kliore, A., Cain, D. L., Levy, G. S., Eshleman, V. R., Fjeldbo, G., & Drake, F. D. (1965).  
367 Occultation experiment: Results of the first direct measurement of Mars's atmosphere and  
368 ionosphere. *Science*, 149(3689), 1243-1248.
- 369 Kliore, A. J., Anabtawi, A., & Nagy, A. F. (2001, December). The ionospheres of Europa,  
370 Ganymede, and Callisto. In *AGU Fall Meeting Abstracts* (Vol. 2001, pp. P12B-0506).
- 371 Ligier, N., Paranicas, C., Carter, J., Poulet, F., Calvin, W. M., Nordheim, T. A., ... & Ferellec, L.  
372 (2019). Surface composition and properties of Ganymede: Updates from ground-based  
373 observations with the near-infrared imaging spectrometer SINFONI/VLT/ESO. *Icarus*, 333, 496-  
374 515.
- 375 Marini, J. W. (1971). The effect of satellite spin on two-way Doppler range-rate  
376 measurements. *IEEE Transactions on Aerospace and Electronic Systems*, (2), 316-320.
- 377 McGrath, Melissa A., et al. "Satellite atmospheres." *Jupiter: The Planet, Satellites and*  
378 *Magnetosphere* (2004): 457-483.
- 379 Phipps, P. H., & Withers, P. (2017). Radio occultations of the Io plasma torus by Juno are  
380 feasible. *Journal of Geophysical Research: Space Physics*, 122(2), 1731-1750.
- 381 Phinney, R. A., & Anderson, D. L. (1968). On the radio occultation method for studying planetary  
382 atmospheres. *Journal of Geophysical Research*, 73(5), 1819-1827.
- 383 Roth, L., Ivchenko, N., Gladstone, G. R., Saur, J., Grodent, D., Bonfond, B., ... & Retherford, K.  
384 D. (2021). A sublimated water atmosphere on Ganymede detected from Hubble Space Telescope  
385 observations. *Nature Astronomy*, 5(10), 1043-1051.

386 Schinder, P. J. (2020). Users Guide for the Cassini Radio Science ionospheric electron density  
 387 profiles data set for both Saturn and Titan.  
 388 [https://atmos.nmsu.edu/data\\_and\\_services/atmospheres\\_data/Cassini/logs/CasRSS\\_ionospheres](https://atmos.nmsu.edu/data_and_services/atmospheres_data/Cassini/logs/CasRSS_ionospheres_profiles_users_guide.pdf)  
 389 [profiles\\_users\\_guide.pdf](https://atmos.nmsu.edu/data_and_services/atmospheres_data/Cassini/logs/CasRSS_ionospheres_profiles_users_guide.pdf)

390 Withers, P. (2020). Revised predictions of uncertainties in atmospheric properties measured by  
 391 radio occultation experiments. *Advances in Space Research*, 66(10), 2466-2475.



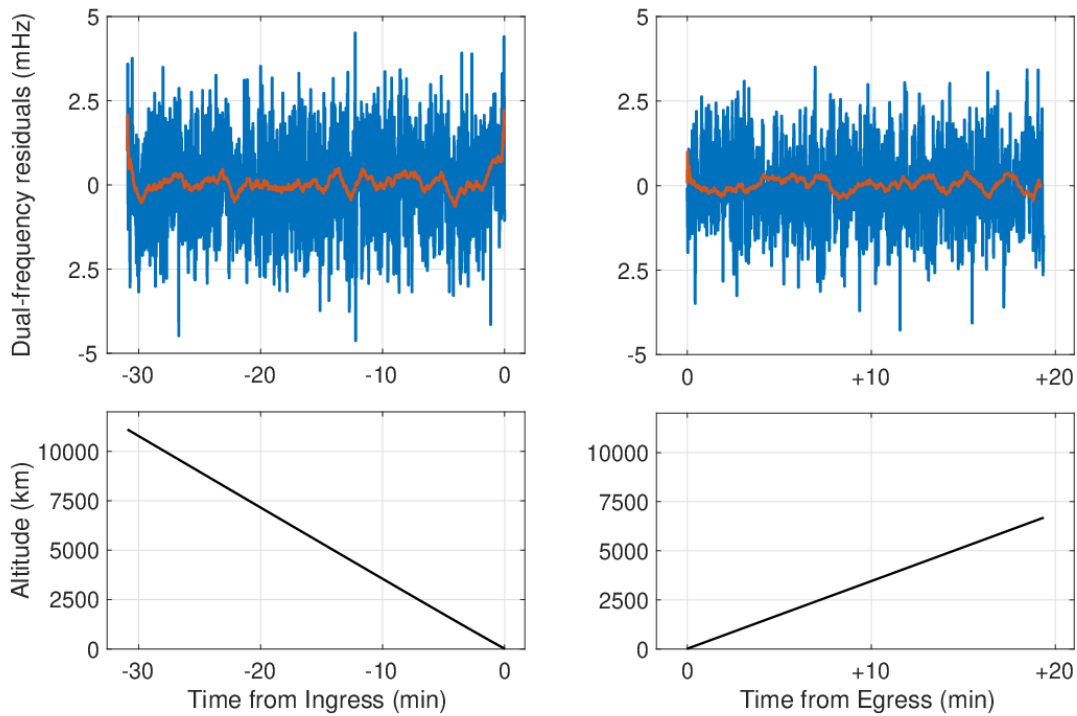
392

393 **Figure 1.** Geometry of the Juno G-34 flyby and radio occultation points. The occultation ingress  
 394 point was just outside the terminator at  $-142^{\circ}\text{W} / 59^{\circ}\text{S}$  and egress occurred just inside the  
 395 terminator near the spacecraft ground track at  $38^{\circ}\text{W} / 20^{\circ}\text{N}$ . The spacecraft ground track is shown

396 in white, sun terminator in yellow, and sub-Jovian point in orange. Overlaid in light red are the  
 397 open/closed field line boundaries from Duling et al (2022).

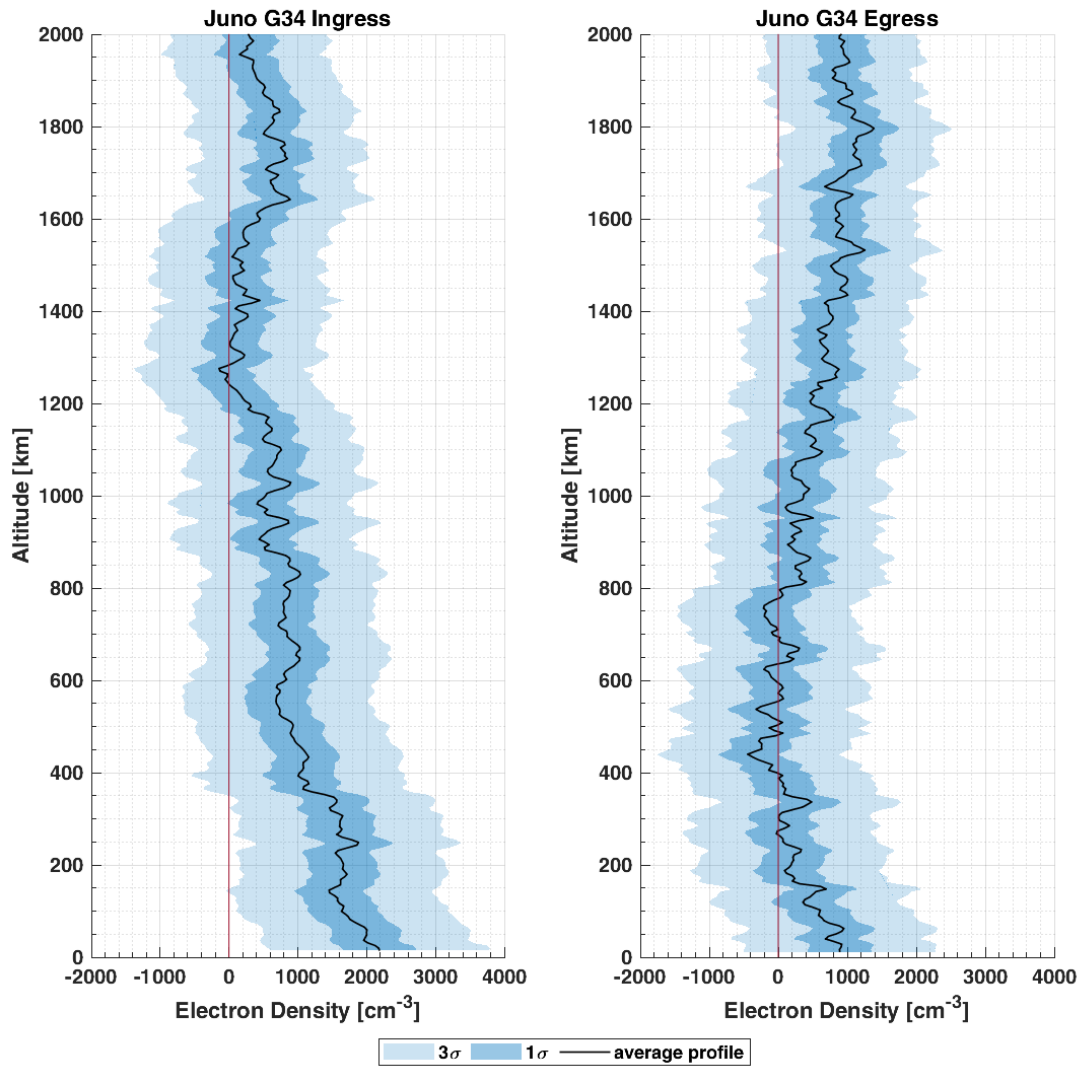
398 **Table 1.** Geometry of the Juno radio occultation of Ganymede. Parameters are given at the  
 399 occultation point (closest point along the radio propagation path to Ganymede).

Observation	Occultation (UTC Earth Receive)	Time	Distance (km)	Lat. (deg)	W. Long. (deg)	Solar Zenith Angle (deg)	Ram Angle (deg)
Juno G34 Ingress	2021-Jun-07 17:18:57		18,094	59° S	-142° W	95°	72°
Juno G34 Egress	2021-Jun-07 17:32:38		3,772	20° N	38° W	80°	125°



400

401 **Figure 2.** Plots of the 1-second integration time (blue) and 60-second average (red) dual-frequency  
 402 residuals (Hz) for the ingress (a) and egress (b) occultations as a function of time, along with plots  
 403 of the ray path altitude over the surface of Ganymede (c, d), during the occultations.



404

405 **Figure 3.** Electron density within Ganymede's ionosphere during ingress occultation (a) and  
 406 egress occultation (b). The dark and light blue shaded area represent the 1- $\sigma$  and 3- $\sigma$  uncertainties,  
 407 respectively.